Deep-ultraviolet Fourier ptychography (DUV-FP) for label-free biochemical imaging via feature-domain optimization

View Online   Export Citation   CrossMark

Qianhao Zhao,[1] Ruihai Wang,[1] Shuhe Zhang,[2] Tianbo Wang,[1] Pengming Song,[1] and Guoan Zheng[1,3,a]

AFFILIATIONS

[1] Department of Biomedical Engineering, University of Connecticut, Storrs, Connecticut 06269, USA
[2] University Eye Clinic Maastricht, Maastricht University Medical Center, Maastricht AZ 6202, The Netherlands
[3] Center for Biomedical and Bioengineering Innovation, University of Connecticut, Storrs, Connecticut 06269, USA

Note: This paper is part of the APL Photonics Special Topic on Photonics in Biomedicine.
[a] Author to whom correspondence should be addressed: guoan.zheng@uconn.edu

ABSTRACT

We present deep-ultraviolet Fourier ptychography (DUV-FP) for high-resolution chemical imaging of biological specimens in their native state without exogenous stains. This approach uses a customized 265-nm DUV LED array for angle-varied illumination, leveraging the unique DUV absorption properties of biomolecules at this wavelength region. We implemented a robust feature-domain optimization framework to overcome common challenges in Fourier ptychographic reconstruction, including vignetting, pupil aberrations, stray light problems, intensity variations, and other systematic errors. By using a 0.12 numerical aperture low-resolution objective lens, our DUV-FP prototype can resolve the 345-nm linewidth on a resolution target, demonstrating at least a four-fold resolution gain compared to the captured raw images. Testing on various biospecimens demonstrates that DUV-FP significantly enhances absorption-based chemical contrast and reveals detailed structural and molecular information. To further address the limitations of conventional FP in quantitative phase imaging, we developed a spatially coded DUV-FP system. This platform enables true quantitative phase imaging of biospecimens with DUV light, overcoming the non-uniform phase response inherent in traditional microscopy techniques. The demonstrated advancements in high-resolution, label-free chemical imaging may accelerate developments in digital pathology, potentially enabling rapid, on-site analysis of biopsy samples in clinical settings.

I. INTRODUCTION

Histological staining is an essential tool for visualizing cellular structures and studying biological processes. Traditional imaging methods heavily rely on exogenous labels and dyes, such as hematoxylin and eosin (H&E) staining and fluorescent dyes to provide contrast and specificity.[1,2] While highly informative, these labeling techniques have several limitations. The staining process can disrupt the native cellular environment, potentially altering the structures and dynamics under investigation.[3] Exogenous labels may also interfere with downstream molecular analyses.[4] Furthermore, the chemicals used for staining can be hazardous, and sample preparation is often laborious and time-consuming.[5,6] To overcome these challenges, there has been increasing interest in developing label-free imaging modalities capable of visualizing biological specimens in their native, unperturbed state. Various label-free imaging techniques have been explored, each exploiting different intrinsic properties of biological samples to generate contrast. For example, quantitative phase imaging (QPI) utilizes the phase shift of light passing through a sample to map the optical path length, enabling visualization of transparent structures without staining.[7–10] Raman spectroscopy and coherent anti-Stokes Raman scattering (CARS) microscopy leverage the inelastic scattering of light to provide chemical fingerprints of molecules, allowing for label-free identification of specific compounds.[11,12] Autofluorescence imaging captures the intrinsic fluorescence of endogenous molecules such as NADH and FAD, providing insights into cellular metabolism.[13,14]

Among these label-free approaches, deep ultraviolet (DUV) microscopy has emerged as a powerful tool for high-contrast imaging of cellular structures. DUV microscopy exploits the intrinsic absorbance of biomolecules at ultraviolet wavelengths, particularly nucleic acids and proteins, which exhibit strong absorption in the DUV range due to their aromatic ring structures.[15,16] DUV microscopy enables detailed visualization of cellular components without the need for exogenous stains. This non-invasive technique allows for real-time study of living cells and tissues[17,18] and has been applied to various biological samples, including quantification of nucleic acids and proteins in cells,[19,20] label-free hematology analysis,[21,22] and rapid histopathological imaging of cancer specimens.[23] The combination of DUV excitation with nonlinear microscopy techniques has further enhanced the capabilities of label-free imaging. These hybrid approaches leverage the intrinsic contrast provided by DUV excitation while exploiting the unique advantages of nonlinear microscopy, such as improved depth penetration and reduced photodamage. Two-photon and three-photon excitation combined with DUV excitation have been employed to study serotonin distribution in living cells and tissues[24,25] and visualize skin vasculature in living mice.[26]

To further enhance the capabilities of DUV microscopy, we propose integrating it with Fourier ptychography (FP),[27] a computational imaging technique that overcomes the resolution limits of traditional microscopy. In a typical microscopy implementation, FP captures multiple low-resolution images under different illumination angles and computationally synthesizes them in the Fourier domain to reconstruct a high-resolution, wide-field complex image of the specimen.[28–33] In the past years, FP has been successfully applied to various imaging applications, including phase contrast imaging of cells and tissues,[30,34–41] digital pathology,[42–46] high-throughput cytometry,[47] reflection-based metrology,[37,48–50] remote sensing,[51–57] and x-ray nanoscopy,[58,59] among others. Recent advancements in DUV imaging have also explored its potential in high-resolution metrology applications. For instance, Park *et al.* demonstrated a reflective DUV Fourier ptychographic microscopy system capable of imaging nanofeatures, showcasing the technique's promise for semiconductor device characterization.[48]

The integration of DUV microscopy with FP, which we term deep-ultraviolet Fourier ptychography (DUV-FP), offers several unique advantages for label-free bio-imaging. It allows for high-resolution imaging using low numerical aperture (NA) objectives, overcoming the traditional resolution constraints of DUV microscopy.[60] The FP algorithm enables computational correction of aberrations inherent in DUV optics, improving image quality without complex optical components. Moreover, DUV-FP provides quantitative phase imaging,[35,36] offering additional information about cellular structures and dynamics. The technique also features an extended depth of field and digital refocusing capabilities, and when combined with diffraction tomography, it has the potential for 3D imaging of thick tissue sections.[61–67]

Conventional FP reconstructions, however, often suffer from vignetting, pupil aberrations, stray light problems, LED intensity variations, LED positional errors, and others.[68–72] To address these issues, we integrate the feature-domain optimization framework[42,73] for enhancing the robustness and fidelity of FP reconstruction under DUV lighting conditions. By formulating the loss function in the feature domain, where effective image information is extracted by a designed feature extractor, DUV-FP can bypass the undesired influence of vignetting effects, stray light, and systematic errors that often degrade conventional FP reconstructions in the image domain.

Another challenge in conventional FP is the loss of low-frequency phase information during the reconstruction process.[74,75] This issue arises from the non-uniform phase transfer characteristic inherent in microscopy systems, which impedes the conversion of object wavefields into discernible intensity variations. To tackle this issue, we incorporate the concept of spatially coded Fourier ptychography (scFP)[75] for developing a spatially coded DUV-FP system. In this system, we attach a coded surface to the image sensor in the FP setup. The spatial modulation of this coded surface[72,76] ensures a uniform phase response across the entire synthetic bandwidth, improving reconstruction quality and correcting refractive index underestimation issues prevalent in conventional FP.

In this work, we demonstrate the efficacy and versatility of DUV-FP through various biological imaging applications. Our results establish DUV-FP as an enabling tool that opens up new possibilities for studying biological specimens without the need for exogenous labels or disruptive sample preparation. This technique has the potential to accelerate biomedical research by enabling non-invasive, high-resolution investigation of cellular structures and processes in their native state. The integration of feature-domain optimization and spatially coded FP further enhances the capabilities of DUV-FP, ensuring accurate reconstruction of complex wavefronts and addressing the challenges associated with quantitative phase imaging in DUV microscopy.

II. DUV-FP WITH FEATURE-DOMAIN OPTIMIZATION

DUV-FP combines the principles of FP with deep ultraviolet illumination to achieve enhanced imaging capabilities. As shown in Fig. 1(a), the DUV-FP system comprises several specialized components designed to operate effectively in the deep ultraviolet spectrum. The core of the system is a programmable 15×15 flat LED array (Crystal IS KL265-50T-SM-WD) emitting at a central wavelength of 265 nm. This array serves as the illumination source, enabling sequential activation of individual LEDs to provide the angle-varied illumination crucial for the FP technique. The optical path includes a $5\times$, 0.12 NA microscope objective lens (Thorlabs LMU-5X-UVB) built with fused silica. Due to the high costs associated with DUV optics, we employ a fused silica plano-convex lens (Thorlabs LA4102-UV) as the tube lens. While this cost-effective alternative introduces some aberrations compared to a specialized tube lens, our feature-domain optimization approach allows for computational correction of these imperfections. This combination of affordable components and advanced computational techniques enables high-quality imaging results while maintaining an accessible system design. Since the DUV light is invisible to the naked eye, a microscope slide with orange fluorescence particles is used in Fig. 1(b) to visualize the DUV illumination.

During the imaging process, each LED in the array is sequentially activated, illuminating the sample from a different angle. This angle-varied illumination is equivalent to shifting the sample's spectrum in the Fourier domain. The low-NA objective lens acts as a low-pass filter, capturing a small region of this shifted spectrum for
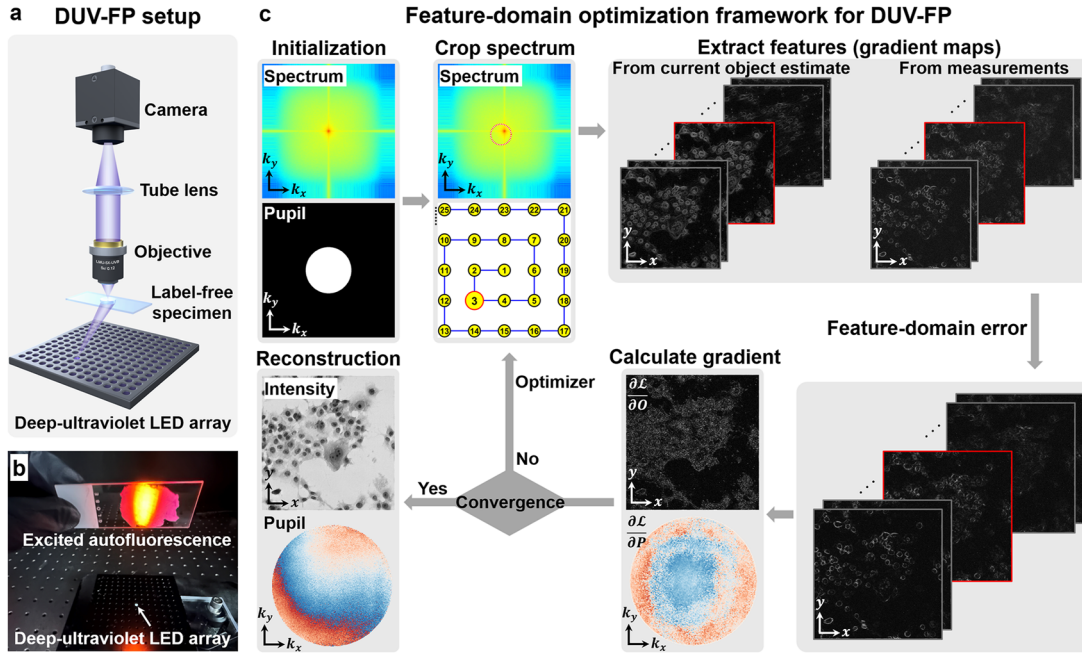
FIG. 1. Deep-ultraviolet Fourier ptychography (DUV-FP) system and feature-domain optimization framework. (a) Schematic of the DUV-FP optical setup, featuring a 15 × 15 LED array (265-nm central wavelength) as the illumination source. (b) Visualization of the DUV illumination using a fluorescent microscope slide. (c) Flowchart of the feature-domain optimization algorithm for DUV-FP. The process includes initialization of the object spectrum and pupil function, spectrum cropping to match LED illumination angles, feature extraction via gradient maps from both the current object estimate and measurements, calculation of feature-domain error, gradient computation for object and pupil updates, and iterative optimization until convergence. The final output includes reconstructed intensity and refined pupil function.

each illumination angle. By acquiring images from multiple illumination angles, DUV-FP effectively expands the system's synthetic NA, resulting in a resolution higher than what the objective lens alone could achieve.

In the DUV-FP setup, the nth LED element emits an incident wave that can be approximated by a tilted plane wave $e^{ik_{xn}x}e^{ik_{yn}y}$ with a wavevector of (k_{xn}, k_{yn}). The complex object $O(x, y)$ interacts with this tilted plane wave, generating an exit field $O(x, y) \cdot e^{ik_{xn}x}e^{ik_{yn}y}$. The objective lens of the system then performs a Fourier transform of this field: $\mathcal{F}\{O(x, y) \cdot e^{ik_{xn}x}e^{ik_{yn}y}\}$ $= \hat{O}(k_x - k_{xn}, k_y - k_{yn})$. The resulting spectrum is low-passed filtered by the pupil aperture $P(k_x, k_y)$ with a cutoff frequency of $NA \cdot 2\pi/\lambda$, where λ is the illumination wavelength. The tube lens performs an inverse Fourier transform of the filtered spectrum and generates a filtered wave field $\varphi_n(x, y)$ at the detector plane. The resulting intensity image $I_n(x, y)$ is then captured by the detector. The forward imaging model of the DUV-FP can be described as[27,72]

$$I_n(x, y) = |\varphi_n(x, y)|^2 = \left| \mathcal{F}^{-1}\{P(k_x, k_y) \cdot \hat{O}(k_x - k_{xn}, k_y - k_{yn})\} \right|^2. \tag{1}$$

We can rewrite the imaging model in the following vectorized form:

$$I_n = |\varphi_n|^2 = \left| \mathcal{F}^{-1}(PM_n\mathcal{F}O) \right|^2. \tag{2}$$

For a complex-valued object $O(x, y)$ of dimensions $A \times A$ in Eq. (1), the vectorized form O in Eq. (2) is a column vector with A^2 elements.

$\mathcal{F}$ and $\mathcal{F}^{-1}$ in Eq. (2) represent the Fourier transform matrix and its inverse, respectively. M_n in Eq. (2) is a spectrum selection matrix for the nth LED element. It has a dimension of $B^2 \times A^2$ with binary values to extract the Fourier spectrum corresponding to the nth LED element, as shown in the "Crop spectrum" panel in Fig. 1(c). Given our resolution enhancement factor of 4, the pupil function P is a diagonal matrix of dimension $B^2 \times B^2$ ($B = A/4$), with the diagonal elements corresponding to actual pupil function values in Eq. (1). The resulting vectorized wave field at the detector plane φ_n and the captured intensity I_n in Eq. (2) are column vectors of dimension B^2. In the actual reconstruction process, there is no need to explicitly compute the matrices in Eq. (2); instead, they can be treated as operators acting on the images.

Figure 1(c) illustrates the flowchart for the feature-domain optimization framework, which can enhance the robustness and fidelity of FP reconstruction under DUV lighting conditions. The key distinction between this framework and traditional FP recovery lies in the transformation of the reconstruction process from the spatial domain to the feature domain.[42,73] This approach effectively mitigates the influence of vignetting, background stray light, and other errors that cause intensity distribution discrepancies. With the vectorized form in Eq. (2), we can define the feature-domain loss function as follows:

$$Loss(O, P) = \sum_{n=1}^{N} \left| \nabla\sqrt{I_n} - \nabla|\varphi_n| \right|, \tag{3}$$

where ∇ represents the first-order gradient of the image, and $|\cdots|$ denotes $\ell 1$ norm. To efficiently leverage the information from the captured data, a mini-batch strategy is employed, with the index n ranging from 1 to N to facilitate stochastic optimization. The loss function in Eq. (3) quantifies the feature domain error by comparing the gradients of the measured amplitude, $\nabla\sqrt{I_n}$, with the gradients of the amplitudes of the predicted light wave at the detector plane, $\nabla|\varphi_n|$. For the reconstruction process, we aim to find a revision to the complex object and the pupil function that reduces this error. The reconstruction algorithm proceeds by calculating the gradients of the loss function with respect to the sample O and pupil function P, as given by the following equations:[42]

$$\frac{\partial \mathcal{L}oss}{\partial O} = \mathcal{F}^{\dagger} \sum_{n=1}^{N} M_n^T P^{\dagger} \mathcal{F}\left(\mathrm{Diag}\left[\nabla^T \mathrm{sign}\left(\nabla\sqrt{I_n} - \nabla|\varphi_n| \right) \right] \frac{\varphi_n}{|\varphi_n|} \right),$$ (4)

$$\frac{\partial \mathcal{L}oss}{\partial P} = \sum_{n=1}^{N} (M_n \mathcal{F}O)^{\dagger} \mathcal{F}\left(\mathrm{Diag}\left[\nabla^T \mathrm{sign}\left(\nabla\sqrt{I_n} - \nabla|\varphi_n| \right) \right] \frac{\varphi_n}{|\varphi_n|} \right),$$ (5)

where $\dagger$ denotes the conjugate transpose. These gradients guide the iterative updates to O and P, which are performed using the RMSProp optimizer,[77] a variant of stochastic gradient descent that adaptively adjusts learning rates based on the historical gradient magnitudes. Our algorithm is considered converged when the change in the cost function falls below a threshold of 0.1%. Alternatively, like other common Fourier ptychographic implementations, we can simply iterate the process for a predefined number of loops, typically around 10–20. Upon convergence, the algorithm yields high-quality reconstructions of the sample's complex value and the refined pupil function, effectively overcoming limitations associated with traditional image-domain phase retrieval methods.

III. IMAGING PERFORMANCE OF DUV-FP

To evaluate the capabilities of our DUV-FP system, we conducted a performance analysis using a USAF resolution target. This standardized target enables precise quantification of resolution improvements and facilitates direct comparison with other common state-of-the-art reconstruction algorithms. Our experimental setup consisted of a 15×15 DUV LED array positioned ~75 mm from the sample, creating a maximum synthetic NA of ~0.5. For
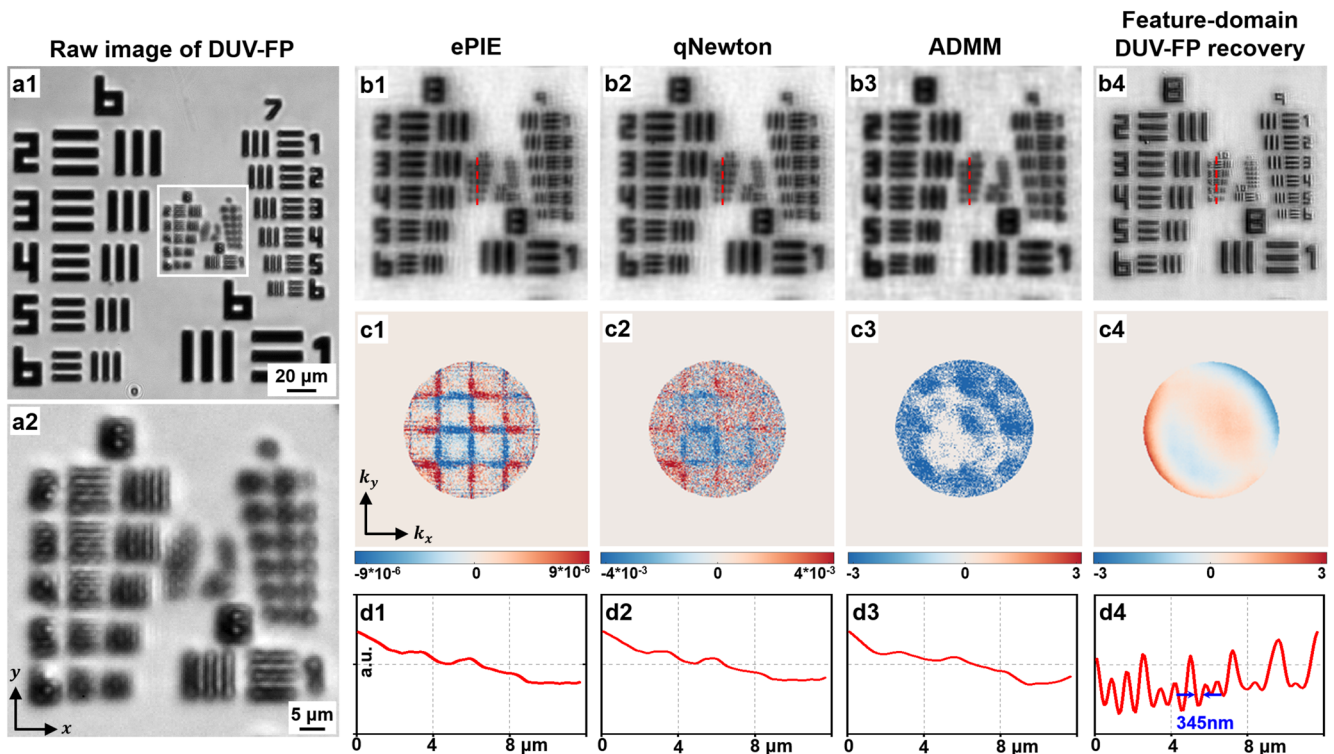
FIG. 2. Imaging performance characterization using a USAF resolution target. (a1) The raw image captured under illumination from the central LED element. (a2) A zoomed-in view of the region marked by the white square in (a1), showing the resolvable features of the target. One can resolve the 1.74-μm linewidth of group 8, element 2 element. (b1)–(b4) Zoomed-in views of the recovered high-resolution images using different reconstruction algorithms: (b1) ePIE, (b2) qNewton, (b3) ADMM, and (b4) the feature-domain framework. (c1)–(c4) Corresponding recovered pupil functions for each reconstruction algorithm. (d1)–(d4) Intensity line traces along the red lines indicated in (b1)–(b4), demonstrating the resolution improvement achieved by each method. The feature-domain framework in (d4) exhibits the best resolution, resolving features down to group 10, element 4, with a 345-nm linewidth. The theoretical resolution of reconstruction corresponds to ~330 nm linewidth on the target. The demonstrated resolution is in good agreement with the theoretical value.

image acquisition, we sequentially activated LEDs corresponding to brightfield illumination, then skipped every other LED element for darkfield illumination. This approach resulted in the capture of ~120 images. While it is possible to further reduce the number of acquisitions, our primary focus in this work was to demonstrate the superior label-free imaging contrast achievable with DUV-FP. Future directions for optimizing imaging speed and quality include exploring ring-format LED arrangements, angling the LED element toward the sample, developing adaptive illumination strategies, and investigating multiplexed illumination techniques.[78–82]

It is important to note that the spectral bandwidth of our DUV LED source, ~15 nm, can affect image quality and resolution. This bandwidth introduces a degree of temporal incoherence, potentially causing slight blurring in the raw images. However, our feature-domain optimization framework demonstrates inherent robustness to such issues. Future improvements could involve modeling the blurring effect using multiple coherent states,[83,84] more accurately accounting for the imaging system's partial coherence, and potentially enhancing resolution and image quality.

Figure 2(a1) presents the raw image obtained under illumination from the central LED, with a magnified view in Fig. 2(a2), where we can resolve the 1.74-μm linewidth on group 8, element 2. To benchmark the feature-domain framework in DUV-FP, we compared its performance against other common FP recovery methods, namely extended ptychographical iterative engine (ePIE),[85,86] quasi-Newton (qNewton),[80] and alternating direction method of multipliers (ADMMs).[87] Figures 2(b1)–2(b4) showcase the reconstructed images from each method, while Figs. 2(c1)–2(c4) display their corresponding recovered pupil functions. Quantitative analysis of the reconstruction quality was performed by generating intensity line traces for group 10 of the recovered target images

[Figs. 2(d1)–2(d4)]. This analysis reveals the performance of the feature-domain optimization framework that accurately resolves features down to group 10, element 4, corresponding to a linewidth of 345 nm. The apparent underperformance of the conventional image-domain methods can be attributed to their sensitivity to systematic errors, such as residual aberrations and misalignments in our setup. In particular, recovering the correct pupil aberration using image-domain methods is challenging. In contrast, our feature-domain approach demonstrates robust handling of complex aberrations and systematic errors inherent in DUV microscopy. This performance highlights the method's resilience to experimental imperfections that may more severely affect image-domain methods under similar conditions.

IV. LABEL-FREE CHEMICAL IMAGING

The use of 265 nm illumination in our DUV-FP system is particularly advantageous for imaging biological samples, as it coincides with the absorption peak of nucleic acids, enhancing contrast and resolution of nuclear features. To demonstrate the potential of DUV-FP for quantitative, label-free chemical imaging of biological samples, we applied our system to three distinct specimen types: unstained HeLa cells, unstained blood smears, and unstained pathology sections. This diverse selection showcases the versatility and effectiveness of DUV-FP across various biological contexts.

We first recovered wide-field, high-resolution images of unstained HeLa cells. Figure 3(a) presents the reconstructed intensity image, showcasing the technique's ability to visualize detailed morphological information without the need for exogenous contrast agents. Notably, the DUV-FP reconstructions reveal well-defined nuclear boundaries, which are barely discernible in conventional
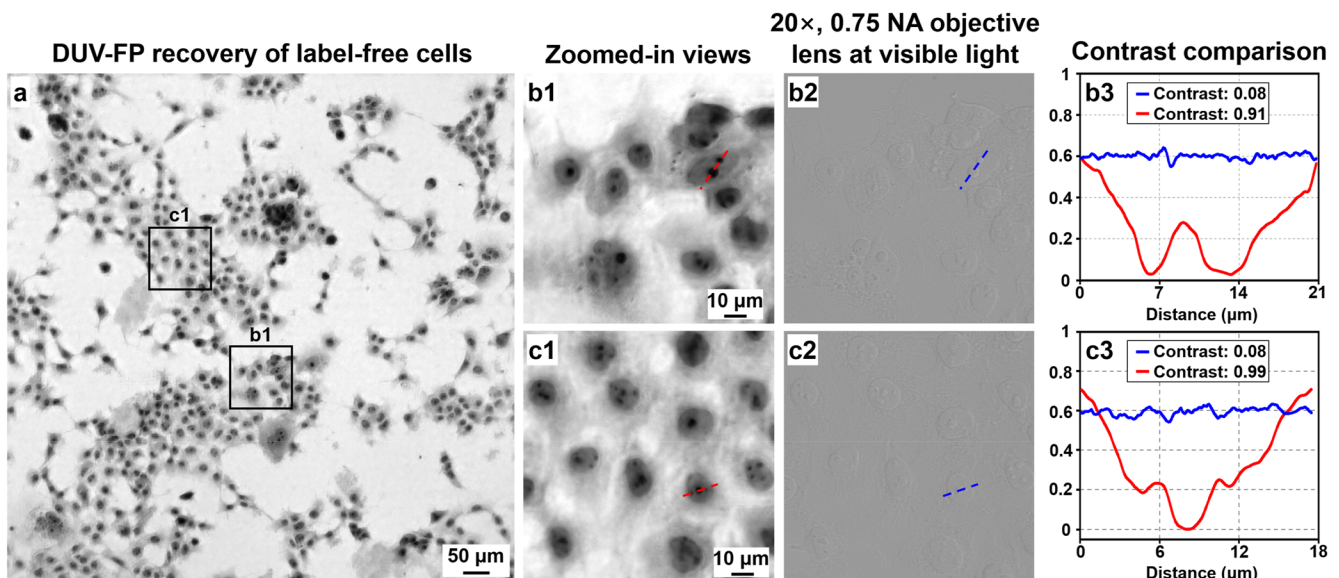
FIG. 3. High-resolution reconstruction of unstained HeLa cells using DUV-FP. (a) Reconstructed intensity image of the HeLa cells. (b1) and (c1) The zoomed-in views of the recovered high-resolution image. (b2) and (c2) The corresponding conventional light microscope images of the same regions. (b3) and (c3) Contrast comparisons between the line traces in the DUV-FP recovered images and the conventional light microscope images. The DUV-FP images exhibit significant contrast enhancement thanks to the intrinsic absorption of biomolecules at the DUV wavelength region.

light microscope images using a regular 20×, 0.75 NA objective lens. The high contrast of nuclear features can be attributed to the strong absorption of 265 nm light by nucleic acids, resulting in a substantial difference in optical density between nuclear and cytoplasmic regions. Zoomed-in views of two regions of interest further illustrate the superior contrast achieved by DUV-FP, as shown in Figs. 3(b1) and 3(c1). In contrast, Figs. 3(b2) and 3(c2) depict images captured by a conventional visible light microscope, where little contrast is observed in the unstained sample.

To quantify the imaging performance, we compared the contrast of line traces drawn across nuclear features in the DUV-FP reconstructions and the conventional light microscope images. The contrast was calculated using the following equation:

$$Contrast = \frac{I_{\max} - I_{\min}}{I_{\max} + I_{\min}}. \qquad (6)$$

In the region of Fig. 3(b1), the DUV-FP reconstruction achieved a contrast of 0.91, significantly higher than the 0.08 contrast of the conventional microscope image in Fig. 3(b3). Similarly, in the region of Fig. 3(c1), the DUV-FP reconstruction yielded a contrast of 0.99, surpassing the 0.08 contrast of the conventional microscope image in Fig. 3(c3). These results underscore the superior contrast-enhancing capabilities of DUV-FP, particularly for visualizing nuclear structures in unstained biological samples.

We next applied DUV-FP to imaging unstained fish blood smears, which are particularly interesting due to the presence of nuclei in fish red blood cells.[88] Figure 4(a) presents the reconstructed intensity image, showcasing a dense distribution of fish red blood cells, each containing a distinct nucleus. Detailed analysis of two regions of interest is presented in Figs. 4(b1) and 4(c1), enabling

clear visualization of nuclear features within individual cells. In contrast, corresponding conventional visible light microscope images [Figs. 4(b2) and 4(c2)] fail to provide sufficient resolution and contrast to discern these details. To quantitatively assess the nuclear features, we employed a dynamic threshold segmentation algorithm to precisely delineate the nuclei in the DUV-FP reconstructed images. The segmentation results in Figs. 4(b1) and 4(c1) demonstrate the algorithm's ability to accurately extract nuclear boundaries in the presence of varying contrast. This segmentation enables the quantification of nuclear size, shape, and chromatin distribution, which are essential parameters for understanding the functional and developmental aspects of fish red blood cells.

The superior contrast achieved by DUV-FP is also evident in this experiment when comparing line traces across nuclear features in the reconstructed images and their conventional light microscope counterparts. Figure 4(b3) presents the intensity profiles along a line crossing a nucleus in Fig. 4(b1) with the DUV-FP reconstruction yielding a contrast of 0.81, substantially higher than the 0.07 contrast observed in the corresponding conventional light microscope image. Similarly, Fig. 4(c3) demonstrates the enhanced contrast of 0.67, surpassing the 0.05 contrast obtained from the conventional light microscope image of the same region. These results underscore the remarkable contrast enhancement provided by DUV-FP, which is crucial for the detailed analysis of nuclear morphology and chromatin distribution within unstained live cells.

We also applied our technique to the imaging of unstained pathology sections. Figure 5 showcases the application of DUV-FP for high-resolution, label-free imaging of two distinct unstained pathology sections (skin tissue sections). The reconstructed intensity images are displayed in Figs. 5(a1) and 5(b1), revealing fine
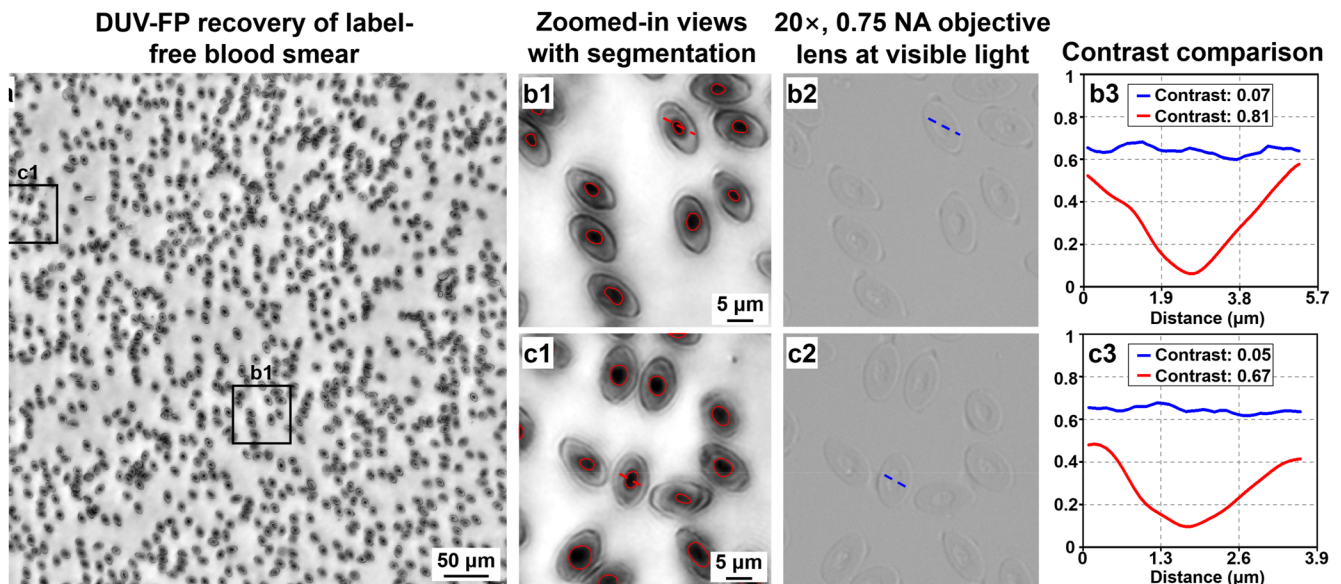
FIG. 4. High-resolution reconstruction of an unstained blood smear using DUV-FP. (a) Reconstructed intensity image of the fish blood cells. (b1) and (c1) The zoomed-in views of the recovered high-resolution image with automatic cell nuclear segmentation, demonstrating the technique's precision in delineating nuclear boundaries. (b2) and (c2) The corresponding conventional light microscope images of the same regions. (b3) and (c3) Contrast comparison between the line traces in the DUV-FP recovered images and the conventional light microscope images.
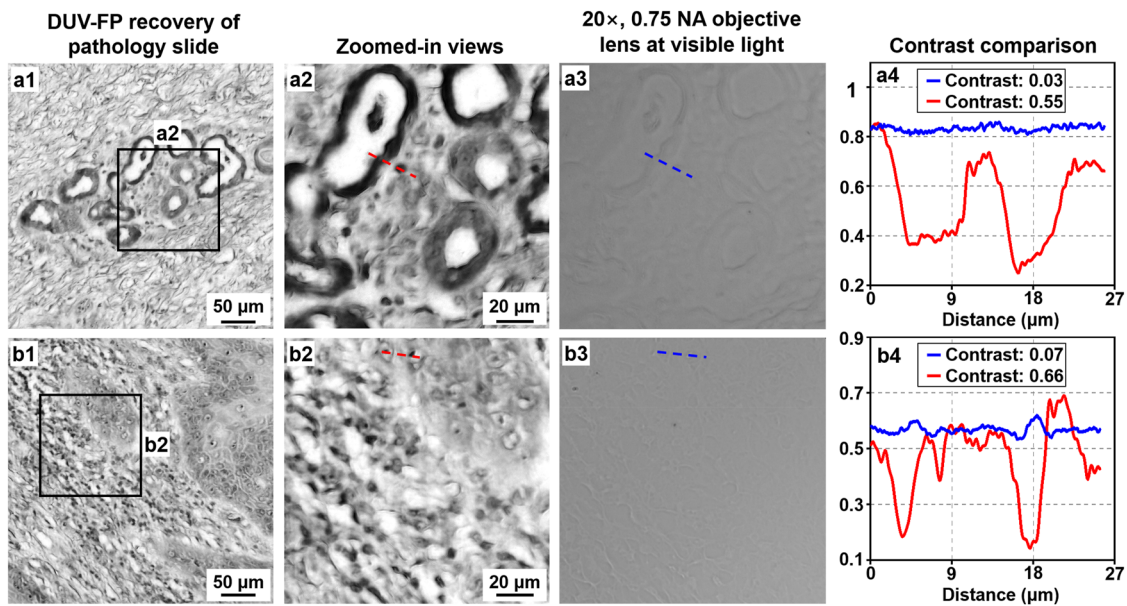
FIG. 5. High-resolution reconstruction of an unstained pathology section using DUV-FP. (a1) and (b1) The reconstructed intensity images of two different pathology sections. (a2) and (b2) The zoomed-in views of the intensity images (a1) and (b1). (a3) and (b3) The corresponding conventional light microscope images of the same regions as (a2) and (b2). (a4) and (b4) Contrast comparison between the intensity line traces in the DUV-FP recovered images and the conventional light microscope images.

morphological details that were previously unresolvable with standard light microscopy. Closer inspection within these sections in Figs. 5(a2) and 5(b2) highlights the high-resolution intensity images recovered through DUV-FP. For comparative analysis, Figs. 5(a3) and 5(b3) show the corresponding conventional light microscope images of the regions, which are captured by a 20×, 0.75 NA objective lens. These conventional microscope images serve as a baseline, illustrating the limitations in image contrast of light microscopy when imaging unstained tissue sections. The DUV-FP images show a remarkable improvement in contrast, as demonstrated by the contrast values calculated from line traces across the images. Specifically, the DUV-FP image of the first section, shown in Fig. 5(a2), achieves a contrast value of 0.55, whereas the corresponding microscope image in Fig. 5(a3) yields a significantly lower contrast of 0.03. Similarly, the second section's DUV-FP image, presented in Fig. 5(b2), exhibits a contrast value of 0.66, compared to 0.07 for the microscope image shown in Fig. 5(b3). These results highlight the superior contrast-enhancing capabilities of DUV-FP in visualizing unstained pathology sections.

The high-resolution, label-free imaging capability of DUV-FP holds great promise for various clinical applications, particularly in the context of rapid, intraoperative pathology consultation. By enabling the visualization of cellular and subcellular details in unstained tissue sections, DUV-FP could potentially accelerate the diagnostic process and guide surgical decision-making in real time. The enhanced contrast and resolution provided by DUV-FP may also facilitate the detection of subtle morphological abnormalities that might be missed with conventional microscopy techniques, ultimately improving the accuracy and reliability of pathological assessment.

In the current study, we employed a low-NA objective lens for image acquisition to demonstrate the resolution enhancement capability of DUV-FP. Looking ahead, the implementation of DUV-FP with a high-NA objective lens offers the potential to further push the boundaries of resolution. By combining the synthetic aperture approach of FP with a high NA objective, it may be possible to achieve an effective NA of up to ~2,[32,89,90] potentially enabling unprecedented levels of detail in label-free biological imaging. This advancement could open new avenues for studying subcellular structures and dynamics at nanoscale resolution, further expanding the utility of DUV-FP in both research and clinical settings.

V. QUANTITATIVE PHASE IMAGING WITH SPATIALLY CODED DUV-FP

Conventional FP faces challenges in recovering accurate quantitative phase information, particularly for low spatial frequencies. This limitation stems from the non-uniform phase transfer characteristic inherent in microscopy systems. When imaging a specimen with any linear phase ramp, which corresponds to a single spatial frequency in Fourier space, conventional FP and other common phase retrieval approaches produce intensity images with constant values across different illumination angles.[75] The phase transfer function (PTF) of conventional FP is essentially zero for any given spatial frequency of phase or a combination thereof. This means that phase information at certain spatial frequencies is permanently lost during data acquisition and cannot be recovered post-measurement. As a result, conventional FP struggles to provide true quantitative phase imaging, particularly for slowly varying phase objects or large, contiguous structures.

To address these limitations, we can integrate the concept of coded ptychography[76,91] with DUV-FP, termed spatially coded DUV-FP, to enable quantitative phase imaging with a uniform phase response. This is accomplished through the spatial modulation introduced by a coded surface on top of the image sensor, which effectively converts object phase information into detectable intensity variations and enables the recovery of low-frequency phase information that is typically lost in conventional Fourier ptychography.[75] There is no specific frequency relationship between the coded surface and the sample's frequencies in this implementation. The coded surface in our setup primarily functions to encode the wavefront rather than to shift high-resolution information to a low-resolution passband, as is the case in lensless coded ptychography.[76,91] The resolution limit in our system is still determined by the incident angle of illumination and the NA of the objective lens. The coded surface helps to ensure a uniform phase response across the synthetic bandwidth, enabling accurate quantitative phase imaging but does not directly alter the system's resolution limit. To characterize the transmission profile of the coded layer, we performed a calibration experiment using a blood smear sample as the object. By translating the blood smear to 1521 locations and capturing the corresponding measurements, we pre-calibrated the complex modulation profile of the coded layer. These pre-calibrated modulation profiles serve as the initial guess of the coded layer in the feature-domain Fourier ptychographic reconstruction process.

The spatially coded DUV-FP reconstruction algorithm, illustrated in Fig. 6, extends our feature-domain optimization framework to incorporate the coded surface modulation. The process begins with the initialization of the object spectrum and pupil function. Subsequently, the algorithm crops the spectrum based on the LED positions, simulating the angle-varied illumination characteristic of FP. A key innovation in spatially coded DUV-FP is the coded surface modulation step. After the cropped spectrum passes through the pupil function, the resulting exit wavefront is modulated by the coded surface, introducing a spatially coded phase and amplitude modulation. This step is crucial for converting phase information into detectable intensity variations, enabling the recovery of low-frequency phase content typically lost in conventional FP. The algorithm then extracts features from both the forward model predictions and the actual measurements. We use gradient maps as features, which effectively capture structural information while being less sensitive to global intensity variations. This feature extraction step is pivotal in mitigating the effects of vignetting, background stray light, and other systematic errors that often plague conventional FP reconstructions. The core of the optimization lies in minimizing the feature-domain error between the predicted and measured data. This error drives the calculation of gradients with respect to the object, coded surface, and pupil function. These gradients guide the iterative updates of these parameters, progressively refining the reconstruction. The algorithm iterates through this process until convergence, producing high-fidelity reconstructions of
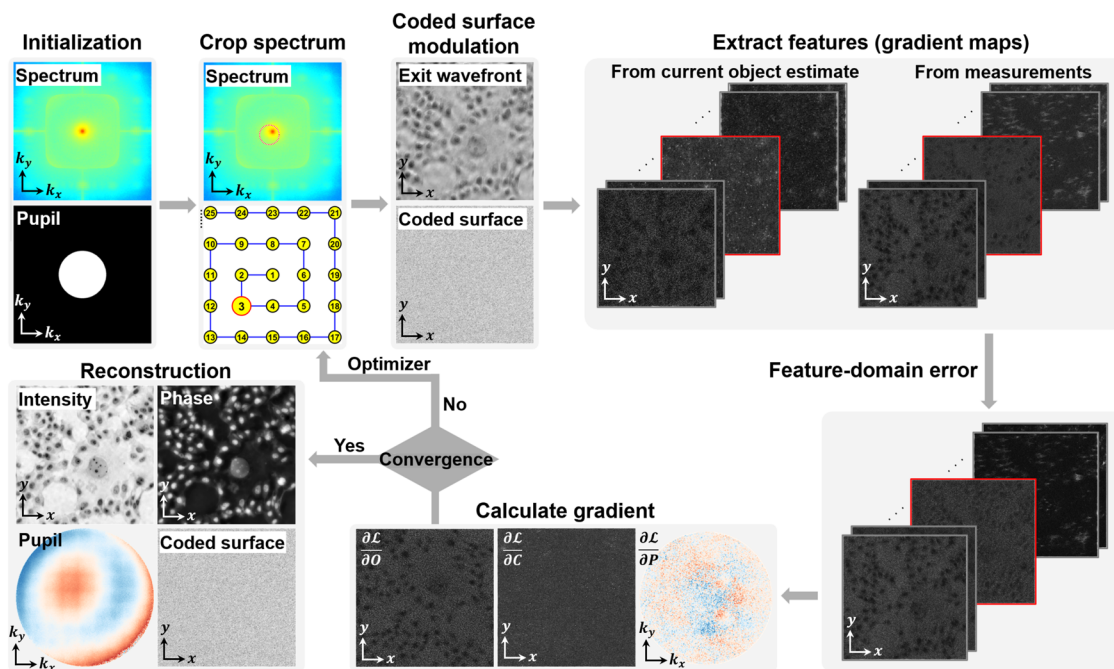

FIG. 6. Extending the feature-domain optimization framework for spatially coded DUV-FP. The algorithm flow includes (1) initialization of spectrum and pupil function, (2) spectrum cropping based on LED positions, (3) coded surface modulation of the exit wavefront, (4) gradient map generation from both current object estimate and measurements, (5) calculation of feature-domain error, and (6) gradient update for object, coded surface, and pupil. The final output includes the reconstructed intensity and phase of the sample, refined pupil function, and updated coded surface profile. This framework enables high-fidelity reconstruction by leveraging spatially coded detection and feature-domain optimization, addressing limitations in conventional FP for quantitative phase imaging.

the sample's intensity and phase, along with refined estimates of the pupil function and coded surface profile (also refer to the Appendix).

The effectiveness of spatially coded FP for quantitative phase imaging has been previously demonstrated,[75] providing compre-

hensive evidence of the technique's ability to achieve a uniform phase response and accurate QPI across a wide range of spatial frequencies. However, in the DUV region, there are no commercially available quantitative phase targets, as conventional
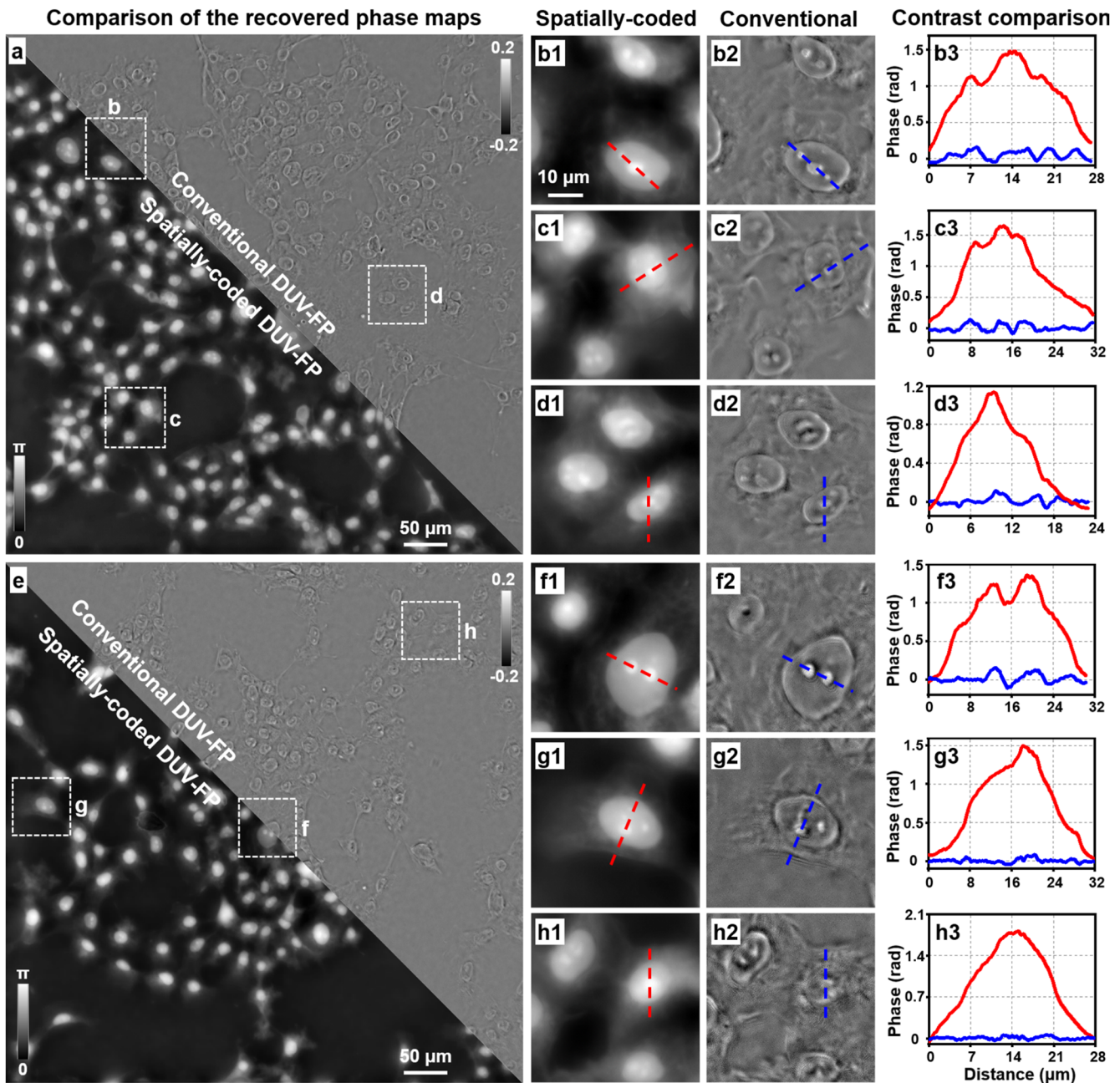
FIG. 7. Comparison of phase reconstructions for HeLa cells using spatially coded DUV-FP and conventional DUV-FP. (a) and (e) Phase maps of two HeLa cell samples, with the left half reconstructed by spatially coded DUV-FP and the right half by conventional DUV-FP. The scales for phase are different for the two approaches. Quantitative contrast comparison can be found in line traces. (b)–(d) and (f)–(h) Zoomed-in views of selected regions of interest from (a) and (e), showing phase reconstructions by spatially coded DUV-FP (b1)–(h1) and conventional DUV-FP (b2)–(h2). (b3)–(h3) Quantitative comparison of phase profiles along the indicated line traces (red for spatially coded DUV-FP, blue for conventional DUV-FP), demonstrating the superior phase contrast and resolution achieved by spatially coded DUV-FP.

phase targets are made on regular glass slides, which are opaque under DUV light illumination. To demonstrate the effectiveness of spatially coded DUV-FP, we performed a phase imaging experiment on HeLa cells. Figure 7 presents the recovered phase maps of two HeLa cell sections, with each image split to directly compare reconstructions from conventional DUV-FP and spatially coded DUV-FP. The spatially coded DUV-FP method consistently produces phase maps with superior contrast and detail, revealing slowly varying phase features across all examined regions. Figures 7(b)–7(d) and 7(f)–7(h) provide zoomed-in views of selected regions of interest, allowing for a more detailed comparison between the two methods. The spatially coded DUV-FP reconstructions in Figs. 7(b1)–7(h1) show significantly enhanced phase contrast compared to conventional DUV-FP in Figs. 7(b2)–7(h2), particularly in resolving intracellular structures and cell boundaries. Analysis of phase profiles in Figs. 7(b3)–7(h3) corroborates these visual observations. The red lines represent spatially coded DUV-FP, while the blue lines show conventional DUV-FP results. Across all regions, spatially coded DUV-FP consistently achieves higher phase shifts with slow-varying phase profiles. These results underscore the potential of spatially coded DUV-FP for enhancing label-free, high-resolution studies of cellular morphology.

VI. DISCUSSION AND CONCLUSION

The development of label-free imaging techniques has long been a crucial goal in biological and medical research, driven by the need to visualize specimens in their native state without the potential disruptions caused by stains or fluorescent markers. Our work addresses the limitations of conventional microscopy methods through the DUV-FP approach. DUV-FP combines the principles of FP with deep ultraviolet illumination, leveraging a feature-domain optimization framework to overcome challenges such as vignetting and systematic errors that have historically plagued FP reconstructions. This approach enables high-resolution, high-contrast imaging of unstained biological samples, as demonstrated in our results with HeLa cells, blood smears, and pathology sections. The significant improvements in contrast and resolution compared to conventional microscopy underscore the potential of DUV-FP in revealing fine cellular structures without the need for staining.

The applications of DUV-FP span a wide range of biomedical research and clinical diagnostics. For instance, the high-contrast imaging of nuclear structures without staining offers new possibilities for studying chromatin organization and nuclear dynamics. In pathology, this technique could revolutionize clinical practice by enabling rapid, intraoperative consultation without time-consuming staining procedures, potentially improving patient outcomes through faster and more informed decision-making during surgeries.

Looking ahead, several avenues for further development and application of DUV-FP warrant exploration. Advancing the technique to achieve even higher resolution could expand its utility in digital pathology and hematology analysis. This optimization may involve exploring DUV illumination with larger incident angles and advanced computational methods, such as neural network-based image reconstruction[92–95] and virtual staining,[14,96] to further enhance image quality, processing speed, and imaging workflow.

Another area for improvement is processing speed. In our current implementation, not yet optimized for parallel computation, the feature-domain approach typically requires 2–5 times longer processing time than conventional ePIE methods. Graphics processing unit (GPU) acceleration is a promising avenue to address this, as the parallel processing capabilities of GPUs are well-suited to compute a batch of gradients in our algorithm. We anticipate that a well-optimized GPU implementation could significantly reduce computation time. Another important aspect for future research is the investigation and mitigation of potential photodamage from deep ultraviolet exposure, particularly for live-cell applications. Developing strategies to minimize photodamage, such as pulsed illumination or the use of protective antioxidants, will be interesting for establishing safe imaging protocols and extending the applicability of DUV-FP to long-term live-cell imaging.[97] Beyond biological applications, DUV-FP could have significant applications in forensic science. For example, it can be combined with ptychographic endoscopy[83] to image regions that are difficult to reach. The high-resolution and label-free nature of DUV illumination could aid in the detection and analysis of minute traces of biological or chemical evidence.

AUTHOR DECLARATIONS
Conflict of Interest

The authors have no conflicts to disclose.

Author Contributions

Q.Z. and R.W. contributed equally to this work.

G.Z. conceived the concept of DUV-FP. Q.Z. and R.W. developed the prototype systems, conducted the experiments, and analyzed the data. S.Z. contributed to the feature-domain optimization framework. All authors contributed to the writing and revision of the paper.

Qianhao Zhao: Data curation (lead); Formal analysis (lead); Methodology (equal); Software (equal); Validation (equal); Visualization (equal); Writing – original draft (equal); Writing – review & editing (equal). **Ruihai Wang**: Data curation (lead); Formal analysis (lead); Methodology (equal); Validation (equal). **Shuhe Zhang**: Writing – review & editing (equal). **Tianbo Wang**: Writing – review & editing (equal). **Pengming Song**: Writing – review & editing (equal). **Guoan Zheng**: Conceptualization (lead); Funding acquisition (lead); Investigation (lead); Methodology (equal); Supervision (lead); Visualization (equal);

Writing – original draft (equal); Writing – review & editing (equal).

DATA AVAILABILITY

The data that support the findings of this study are available from the corresponding author upon reasonable request.

APPENDIX: FORWARD MODEL AND FEATURE-DOMAIN LOSS FUNCTION FOR SPATIALLY CODED DUV-FP

Spatially coded DUV-FP incorporates a coded layer on the image sensor. The distance between the coded layer and the image sensor is d_2. This coded layer is crucial for recovering low-frequency information, which is often lost in conventional FP techniques. Assuming the distance between the sample O and the coded surface profile C is d_1, we can express the forward model as

$$I_n = |\varphi_n|^2 = \left| \mathcal{F}^\dagger D_2 \mathcal{F} C \mathcal{F}^\dagger D_1 P M_n \mathcal{F} O \right|^2, \tag{A1}$$

where $\mathcal{F}$ and $\mathcal{F}^\dagger$ represent the Fourier transform and its inverse, while M_n denotes the selection matrix for the nth LED illumination out of a total of N LEDs, determined by the frequency domain coordinates corresponding to each LED element. φ_n represents the n-th exit wavefront inferred by the forward model for the nth LED. D_1 and D_2 represent the free space propagation operation that propagates the wavefront backward by distances d_1 and d_2, respectively. This forward model illustrates the physical process of spatially coded DUV-FP: the spectrum selected by different selection matrices is low-pass filtered by the pupil function, and the resulting wavefront is propagated to the coded surface. After interacting with the coded surface, it is then propagated to the sensor plane to generate the intensity measurement.

The feature-domain loss function for spatially coded DUV-FP can be defined as

$$Loss(O, P, C) = \sum_{n=1}^{N} \left| \nabla \sqrt{I_n} - \nabla |\varphi_n| \right|. \tag{A2}$$

Here, ∇ represents the first-order gradient of the image. This loss function quantifies the feature domain error by comparing the gradients of the measured amplitude, $\nabla \sqrt{I_n}$, with the gradients of the amplitudes of the predicted exit wavefronts, $\nabla |\varphi_n|$.

To update the sample O, pupil function P, and coded surface profile C using the RMSProp optimizer, we need to calculate their respective gradients,

$$\frac{\partial \mathcal{L}oss}{\partial O} = \mathcal{F}^\dagger \sum_{n=1}^{N} M_n^T P^\dagger D_1^\dagger \mathcal{F} C^\dagger \mathcal{F}^\dagger D_2^\dagger \mathcal{F}$$
$$\times \left(\text{Diag}\left[\nabla^T \text{sign}\left(\nabla \sqrt{I_n} - \nabla |\varphi_n| \right) \right] \frac{\varphi_n}{|\varphi_n|} \right), \tag{A3}$$

$$\frac{\partial \mathcal{L}oss}{\partial P} = \sum_{n=1}^{N} (M_n \mathcal{F} O)^\dagger D_1^\dagger \mathcal{F} C^\dagger \mathcal{F}^\dagger D_2^\dagger \mathcal{F}$$
$$\times \left(\text{Diag}\left[\nabla^T \text{sign}\left(\nabla \sqrt{I_n} - \nabla |\varphi_n| \right) \right] \frac{\varphi_n}{|\varphi_n|} \right), \tag{A4}$$

$$\frac{\partial \mathcal{L}oss}{\partial C} = \sum_{n=1}^{N} \left(\mathcal{F}^\dagger D_1 P M_n \mathcal{F} O \right)^\dagger \mathcal{F}^\dagger D_2^\dagger \mathcal{F}$$
$$\times \left(\text{Diag}\left[\nabla^T \text{sign}\left(\nabla \sqrt{I_n} - \nabla |\varphi_n| \right) \right] \frac{\varphi_n}{|\varphi_n|} \right). \tag{A5}$$

With these gradients, the RMSProp optimizer will continue to iteratively optimize the sample O, pupil function P, and coded layer profile C until convergence, ultimately providing the final reconstructions of these unknowns. Figure 8 shows the recovered coded surface profile on the detector.
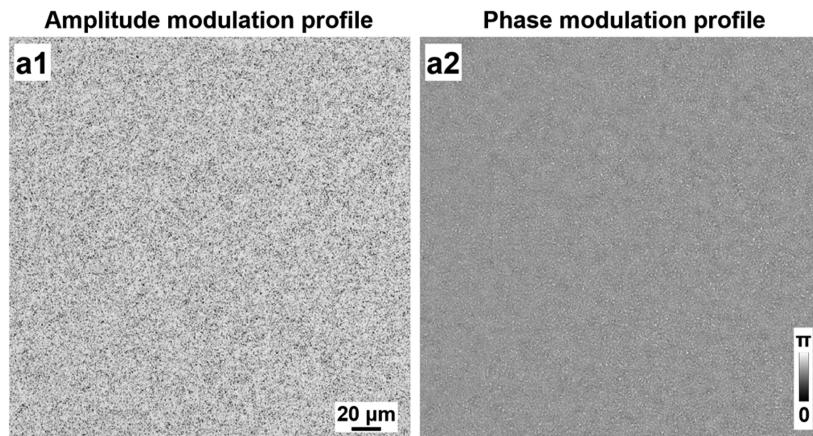

FIG. 8. Recovered complex modulation profile of the coded surface C. (a1) The recovered amplitude modulation profile. (a2) The recovered phase modulation profile.

REFERENCES

[1] A. H. Fischer, K. A. Jacobson, J. Rose, and R. Zeller, Cold Spring Harbor Protoc. **2008**(5), pdb.prot4986.

[2] J. W. Lichtman and J.-A. Conchello, Nat. Methods **2**(12), 910–919 (2005).

[3] U. Schnell, F. Dijk, K. A. Sjollema, and B. N. Giepmans, Nat. Methods **9**(2), 152–158 (2012).

[4] V. Magidson and A. Khodjakov, Methods Cell Biol. **114**, 545–560 (2013).

[5] R. Dixit and R. Cyr, Plant J. **36**(2), 280–290 (2003).

[6] J. A. Ramos-Vara, Vet. Pathol. **42**(4), 405–426 (2005).

[7] Y. Park, C. Depeursinge, and G. Popescu, Nat. Photonics **12**(10), 578–589 (2018).

[8] C. Zuo, J. Li, J. Sun, Y. Fan, J. Zhang, L. Lu, R. Zhang, B. Wang, L. Huang, and Q. Chen, Opt. Lasers Eng. **135**, 106187 (2020).

[9] T. Cacace, V. Bianco, and P. Ferraro, Opt. Lasers Eng. **135**, 106188 (2020).

[10] K. Wang, L. Song, C. Wang, Z. Ren, G. Zhao, J. Dou, J. Di, G. Barbastathis, R. Zhou, J. Zhao, and E. Y. Lam, Light: Sci. Appl. **13**(1), 4 (2024).

[11] A. Ramoji, U. Neugebauer, T. Bocklitz, M. Foerster, M. Kiehntopf, M. Bauer, and J. r. Popp, Anal. Chem. **84**(12), 5335–5342 (2012).

[12] J. P. Pezacki, J. A. Blake, D. C. Danielson, D. C. Kennedy, R. K. Lyn, and R. Singaravelu, Nat. Chem. Biol. **7**(3), 137–145 (2011).

[13] M. Monici, Biotechnol. Annu. Rev. **11**, 227–256 (2005).

[14] Y. Rivenson, H. Wang, Z. Wei, K. de Haan, Y. Zhang, Y. Wu, H. Günaydın, J. E. Zuckerman, T. Chong, A. E. Sisk et al., Nat. Biomed. Eng. **3**(6), 466–477 (2019).

[15] B. J. Zeskind, C. D. Jordan, W. Timp, L. Trapani, G. Waller, V. Horodincu, D. J. Ehrlich, and P. Matsudaira, Nat. Methods **4**(7), 567–569 (2007).

[16] F. Fereidouni, Z. T. Harmany, M. Tian, A. Todd, J. A. Kintner, J. D. McPherson, A. D. Borowsky, J. Bishop, M. Lechpammer, S. G. Demos, and R. Levenson, Nat. Biomed. Eng. **1**(12), 957–966 (2017).

[17] V. Gorti and F. E. Robles, paper presented at the Multiscale Imaging and Spectroscopy IV, 2023.

[18] B. J. Zeskind, Microsc. Microanal. **14**(S2), 740–741 (2008).

[19] M. C. Cheung, J. G. Evans, B. McKenna, and D. J. Ehrlich, Cytometry, Part A **79**(11), 920–932 (2011).

[20] M. C. Cheung, R. LaCroix, B. K. McKenna, L. Liu, J. Winkelman, and D. J. Ehrlich, Cytometry, Part A **83**(6), 540–551 (2013).

[21] A. Ojaghi, G. Carrazana, C. Caruso, A. Abbas, D. R. Myers, W. A. Lam, and F. E. Robles, Proc. Natl. Acad. Sci. U. S. A. **117**(26), 14779–14789 (2020).

[22] A. Ojaghi, E. K. Williams, N. Kaza, V. Gorti, H. Choi, J. Torey, T. Wiley, B. Turner, S. Jackson, S. Park, W. A. Lam, and F. E. Robles, Opt. Lett. **47**(22), 6005–6008 (2022).

[23] S. Soltani, A. Ojaghi, H. Qiao, N. Kaza, X. Li, Q. Dai, A. O. Osunkoya, and F. E. Robles, Sci. Rep. **12**(1), 9329 (2022).

[24] S. Maiti, J. B. Shear, R. Williams, W. Zipfel, and W. W. Webb, Science **275**(5299), 530–532 (1997).

[25] W. R. Zipfel, R. M. Williams, R. Christie, A. Y. Nikitin, B. T. Hyman, and W. W. Webb, Proc. Natl. Acad. Sci. U. S. A. **100**(12), 7075–7080 (2003).

[26] C. Li, R. K. Pastila, C. Pitsillides, J. M. Runnels, M. Puoris'haag, D. Côté, and C. P. Lin, Opt. Express **18**(2), 988–999 (2010).

[27] G. Zheng, R. Horstmeyer, and C. Yang, Nat. Photonics **7**(9), 739–745 (2013).

[28] G. Zheng, C. Shen, S. Jiang, P. Song, and C. Yang, Nat. Rev. Phys. **3**(3), 207–223 (2021).

[29] S. Jiang, P. Song, T. Wang, L. Yang, R. Wang, C. Guo, B. Feng, A. Maiden, and G. Zheng, Nat. Protoc. **18**(7), 2051–2083 (2023).

[30] A. Pan, C. Zuo, and B. Yao, Rep. Prog. Phys. **83**(9), 096101 (2020).

[31] P. C. Konda, L. Loetgering, K. C. Zhou, S. Xu, A. R. Harvey, and R. Horstmeyer, Opt. Express **28**(7), 9603–9630 (2020).

[32] X. Ou, R. Horstmeyer, G. Zheng, and C. Yang, Opt. Express **23**(3), 3472–3491 (2015).

[33] S. Jiang, T. Wang, and G. Zheng, in Coded Optical Imaging, edited by J. Liang (Springer International Publishing, Cham, 2024), pp. 181–203.

[34] X. Ou, R. Horstmeyer, C. Yang, and G. Zheng, Opt. Lett. **38**(22), 4845–4848 (2013).

[35] A. Williams, J. Chung, X. Ou, G. Zheng, S. Rawal, Z. Ao, R. Datar, C. Yang, and R. Cote, J. Biomed. Opt. **19**(6), 066007 (2014).

[36] J. Sun, C. Zuo, L. Zhang, and Q. Chen, Sci. Rep. **7**(1), 1187 (2017).

[37] K. Guo, S. Dong, and G. Zheng, IEEE J. Sel. Top. Quantum Electron. **22**(4), 77–88 (2016).

[38] S. Song, J. Kim, S. Hur, J. Song, and C. Joo, ACS Photonics **8**(1), 158–165 (2021).

[39] L. Tian, Z. Liu, L.-H. Yeh, M. Chen, J. Zhong, and L. Waller, Optica **2**(10), 904–911 (2015).

[40] K. C. Lee, K. Lee, J. Jung, S. H. Lee, D. Kim, and S. A. Lee, ACS Photonics **8**(5), 1307–1315 (2021).

[41] D. Pirone, V. Bianco, M. Valentino, M. Mugnano, V. Pagliarulo, P. Memmolo, L. Miccio, and P. Ferraro, Opt. Lasers Eng. **156**, 107103 (2022).

[42] S. Zhang, A. Wang, J. Xu, T. Feng, J. Zhou, and A. Pan, Optica **11**(5), 634–646 (2024).

[43] M. Liang, C. Bernadt, S. B. J. Wong, C. Choi, R. Cote, and C. Yang, J. Pathol. Inf. **13**, 100119 (2022).

[44] R. Horstmeyer, X. Ou, G. Zheng, P. Willems, and C. Yang, Comput. Med. Imaging Graphics **42**, 38–43 (2015).

[45] J. Chen, A. Wang, A. Pan, G. Zheng, C. Ma, and B. Yao, Photonics Res. **10**(10), 2410–2421 (2022).

[46] M. Valentino, V. Bianco, L. Miccio, P. Memmolo, V. Brancato, P. Libretti, M. Gambacorta, M. Salvatore, and P. Ferraro, Front. Physiol. **14**, 1120099 (2023).

[47] A. C. Chan, J. Kim, A. Pan, H. Xu, D. Nojima, C. Hale, S. Wang, and C. Yang, Sci. Rep. **9**(1), 11114 (2019).

[48] K. S. Park, Y. S. Bae, S.-S. Choi, and M. Y. Sohn, APL Photonics **7**(9), 096105 (2022).

[49] H. Lee, B. H. Chon, and H. K. Ahn, Opt. Express **27**(23), 34382–34391 (2019).

[50] H. Wang, J. Zhu, J. Sung, G. Hu, J. Greene, Y. Li, S. Park, W. Kim, M. Lee, Y. Yang, and L. Tian, Opt. Express **31**(7), 11007–11018 (2023).

[51] S. Dong, R. Horstmeyer, R. Shiradkar, K. Guo, X. Ou, Z. Bian, H. Xin, and G. Zheng, Opt. Express **22**(11), 13586–13599 (2014).

[52] S. Dong, P. Nanda, K. Guo, J. Liao, and G. Zheng, Photonics Res. **3**(1), 19–23 (2015).

[53] J. Holloway, Y. Wu, M. K. Sharma, O. Cossairt, and A. Veeraraghavan, Sci. Adv. **3**(4), e1602564 (2017).

[54] J. Zhang, W. Wei, K. Yang, Q. Zhou, H. Ma, G. Ren, and Z. Xie, APL Photonics **9**(6), 066106 (2024).

[55] S. Divitt, S. Park, H. Gemar, K. P. Judd, H. Dave, D. Lin, D. F. Gardner, and A. T. Watnik, Appl. Opt. **63**(8), C8–C14 (2024).

[56] S. Li, B. Wang, H. Guan, G. Zheng, Q. Chen, and C. Zuo, Adv. Imaging **1**(1), 011005 (2024).

[57] H. Zhang, S. Jiang, J. Liao, J. Deng, J. Liu, Y. Zhang, and G. Zheng, Opt. Express **27**(5), 7498–7512 (2019).

[58] H. Simons, H. F. Poulsen, J. Guigay, and C. Detlefs, arXiv:1609.07513 (2016).

[59] K. Wakonig, A. Diaz, A. Bonnin, M. Stampanoni, A. Bergamaschi, J. Ihli, M. Guizar-Sicairos, and A. Menzel, Sci. Adv. **5**(2), eaav0282 (2019).

[60] A. Faridian, D. Hopp, G. Pedrini, U. Eigenthaler, M. Hirscher, and W. Osten, Opt. Express **18**(13), 14159–14164 (2010).

[61] R. Horstmeyer, J. Chung, X. Ou, G. Zheng, and C. Yang, Optica **3**(8), 827–835 (2016).

[62] C. Zuo, J. Sun, J. Li, A. Asundi, and Q. Chen, Opt. Lasers Eng. **128**, 106003 (2020).

[63] L. Tian and L. Waller, Optica **2**(2), 104–111 (2015).

[64] S. Chowdhury, M. Chen, R. Eckert, D. Ren, F. Wu, N. Repina, and L. Waller, Optica **6**(9), 1211–1219 (2019).

[65] J. Li, A. Matlock, Y. Li, Q. Chen, C. Zuo, and L. Tian, Adv. Photonics **1**(6), 066004 (2019).

[66] S. Song, J. Kim, T. Moon, B. Seong, W. Kim, C.-H. Yoo, J.-K. Choi, and C. Joo, Light: Sci. Appl. **12**(1), 124 (2023).

[67] S. Xu, X. Yang, P. Ritter, X. Dai, K. Chul Lee, L. Kreiss, K. C. Zhou, K. Kim, A. Chaware, J. Neff et al., Adv Photonics **6**(02), 026004 (2024).

[68] A. Pan, C. Zuo, Y. Xie, M. Lei, and B. Yao, Opt. Lasers Eng. **120**, 40–48 (2019).

[69] J. Sun, Q. Chen, Y. Zhang, and C. Zuo, Biomed. Opt. Express **7**(4), 1336–1350 (2016).

[70] R. Eckert, Z. F. Phillips, and L. Waller, Appl. Opt. **57**(19), 5434–5442 (2018).

[71] Z. Bian, S. Dong, and G. Zheng, Opt. Express **21**(26), 32400–32410 (2013).

[72] T. Wang, S. Jiang, P. Song, R. Wang, L. Yang, T. Zhang, and G. Zheng, Biomed. Opt. Express **14**(2), 489–532 (2023).

[73] S. Zhang, T. T. Berendschot, and J. Zhou, Signal Process. **210**, 109088 (2023).

[74] S. Zhou, J. Li, J. Sun, N. Zhou, H. Ullah, Z. Bai, Q. Chen, and C. Zuo, Optica **9**(12), 1362–1373 (2022).

[75] R. Wang, L. Yang, Y. Lee, K. Sun, K. Shen, Q. Zhao, T. Wang, X. Zhang, J. Liu, P. Song, and G. Zheng, Adv. Opt. Mater. **12**, 2303028 (2024).

[76] S. Jiang, C. Guo, P. Song, N. Zhou, Z. Bian, J. Zhu, R. Wang, P. Dong, Z. Zhang, J. Liao, J. Yao, B. Feng, M. Murphy, and G. Zheng, ACS Photonics **8**(11), 3261–3271 (2021).

[77] M. Zaheer, S. Reddi, D. Sachan, S. Kale, and S. Kumar, *Advances in Neural Information Processing Systems*, 31 (NeurIPS, 2018).

[78] K. Guo, S. Dong, P. Nanda, and G. Zheng, Opt. Express **23**(5), 6171–6180 (2015).

[79] Y. Shu, J. Sun, J. Lyu, Y. Fan, N. Zhou, R. Ye, G. Zheng, Q. Chen, and C. Zuo, PhotoniX **3**(1), 24 (2022).

[80] L. Tian, X. Li, K. Ramchandran, and L. Waller, Biomed. Opt. Express **5**(7), 2376–2389 (2014).

[81] P. Song, T. Wang, S. Jiang, C. Guo, R. Wang, L. Yang, Y. Zhou, and G. Zheng, Intell. Comput. **2**, 0015 (2023).

[82] L. Bian, J. Suo, G. Situ, G. Zheng, F. Chen, and Q. Dai, Opt. Lett. **39**(23), 6648–6651 (2014).

[83] P. Song, R. Wang, L. Loetgering, J. Liu, P. Vouras, Y. Lee, S. Jiang, B. Feng, A. Maiden, C. Yang, and G. Zheng, Light: Sci. Appl. **13**(1), 168 (2024).

[84] P. Thibault and A. Menzel, Nature **494**(7435), 68–71 (2013).

[85] A. M. Maiden and J. M. Rodenburg, Ultramicroscopy **109**(10), 1256–1262 (2009).

[86] X. Ou, G. Zheng, and C. Yang, Opt. Express **22**(5), 4960–4972 (2014).

[87] A. Wang, Z. Zhang, S. Wang, A. Pan, C. Ma, and B. Yao, Cells **11**(9), 1512 (2022).

[88] P. Blaxhall and K. Daisley, J. Fish Biol. **5**(6), 771–781 (1973).

[89] M. Liang and C. Yang, Opt. Express **30**(12), 20321–20332 (2022).

[90] J. Sun, C. Zuo, L. Zhang, and Q. Chen, Sci. Rep. **7**(1), 1187 (2017).

[91] S. Jiang, J. Zhu, P. Song, C. Guo, Z. Bian, R. Wang, Y. Huang, S. Wang, H. Zhang, and G. Zheng, Lab Chip **20**(6), 1058–1065 (2020).

[92] S. Jiang, K. Guo, J. Liao, and G. Zheng, Biomed. Opt. Express **9**(7), 3306–3319 (2018).

[93] H. Zhou, B. Y. Feng, H. Guo, S. S. Lin, M. Liang, C. A. Metzler, and C. Yang, Optica **10**(12), 1679–1687 (2023).

[94] C. Guo, S. Jiang, L. Yang, P. Song, T. Wang, X. Shao, Z. Zhang, M. Murphy, and G. Zheng, Opt. Express **29**(24), 39669–39684 (2021).

[95] T. Nguyen, Y. Xue, Y. Li, L. Tian, and G. Nehmetallah, Opt. Express **26**(20), 26470–26484 (2018).

[96] L. Kreiss, S. Jiang, X. Li, S. Xu, K. C. Zhou, K. C. Lee, A. Mühlberg, K. Kim, A. Chaware, M. Ando *et al.*, PhotoniX **4**(1), 34 (2023).

[97] S. Wäldchen, J. Lehmann, T. Klein, S. van de Linde, and M. Sauer, Sci. Rep. **5**(1), 15348 (2015).